Application of PDS-FEM to the Simulation of Dynamic Crack Propagation and Supershear Rupture

†Lionel Quaranta[1,2], Lalith Wijerathne[1,2], Tomoo Okinaka[3] and Muneo Hori[1,2]

[1]Department of Civil Engineering, University of Tokyo, Japan

[2]Earthquake Research Institute, Japan

[3]Department of Civil and Environmental Engineering, Kindai University, Japan

†Corresponding author: lionel@eri.u-tokyo.ac.jp

Abstract

Classical dynamic crack propagation problems are simulated with PDS-FEM, which uses a simple and effective particle-based approach for failure, without the need of a complex treatment of the crack. Two Hamiltonian based formulations are proposed for accurate time integration: the traditional displacement-momentum form and the strain-momentum form, for which consistent momentum conserving and symplectic time integration schemes are derived. Numerical results are verified and validated by comparing with high speed photoelastic observations of a dynamic mode-I crack captured with a 1Mfps camera. Our results show that both methods are successful in reproducing the crack patterns observed experimentally for standard 2D and 3D problems, as well as the variation of the stress distribution around the crack tip during the propagation. The two methods appear numerically indifferentiable although the displacement-based method offers a significantly better computational performance.

We also show that our approach can be applied to the simulation of super-shear rupture in earthquakes. The fault is represented by a crack under mode II loading, and the frictional contact follows a classical slip-weakening law. We could successfully reproduce both the intersonic and sub Rayleigh regimes, in good agreement with the expected rupture velocity ranges for different seismic factors.

Keywords: Brittle failure, dynamic crack propagation, Hamiltonian, PDS-FEM, supershear

Introduction

Predicting the potential impact of extreme events, such as near field supershear earthquakes, on critical infrastructures is a challenging task. It involves shock waves and large-scale dynamic crack propagation simulations, which are computationally demanding, especially in three dimensions. Such simulations require a high degree of accuracy to reproduce a crack path and a crack tip speed consistent with what is observed experimentally, since both are extremely sensitive to the variations of the stress distribution in the material.

An accurate and relatively light numerical method is required to conduct large scale crack propagation simulations, like supershear rupture earthquakes. Adapted advanced discretized methods such as XFEM with level-set [1]-[3] or discontinuous Galerkin methods [4] have been widely used and refined in recent years, leading to a more accurate representation of crack nucleation and propagation. However, most of them involve high numerical overheads, especially in 3D problems, making those difficult to be adapted to large scale simulations. Most 3D studies focus their efforts on the accurate reproduction of the crack path, where the crack is often defined by either cohesive elements/interactions or level-set functions. Recently, Seagraves *et al.* [5] simulated the dynamic crack propagation caused by the impact on brittle plates, where the crack evolution as a function of time is showed to be quite consistent with the experiment. Bede *et al.* [6] conducted a similar simulation for a notched beam fracture modes.

We propose an alternative approach based on PDS-FEM [7]-[10], which uses a simple and effective particle-based approach for failure, without the need of a complex treatment of the crack. Two Hamiltonian based formulations were proposed [11] for accurate time integration:

the traditional displacement-momentum form and the rather new strain-momentum form, for which numerical accuracy and computational efficiency were not yet estimated. In this study the two methods are implemented and compared, both in terms of the accuracy in dynamic crack propagation applications and computational performance.
We also demonstrate that our method can be applied to the simulation of supershear earthquake scenarios. The existence of supershear rupture was first theoretically predicted by Burridge *et al.*[12], and although this result could be subsequently reproduced numerically, in particular by Andrews[13] and Das and Aki[14], actual observations are relatively recent. Rosakis *et al.*[15,16] experimentally reproduced a supershear rupture of Homalite-100 plates, and visualized the characteristic shock wave pattern (Mach cone) with photoelastic fringes. Although rare, several occurrences of supershear fault rupture in earthquakes have been identified, including the 1979 Imperial Valley[17], the 1999 Izmit and Duzce[18], 2001 Kunlun[19], 2002 Denali[20], and more recently the 2018 Palu Earthquake[21]. Understanding the conditions leading to supershear rupture, and the influence on ground motion close and far from the fault, is of particular importance as it will allow the evaluation of the impact on infrastructures, which may be significantly different from that of conventional earthquakes.

Section 1 presents the analytical expressions of the two Hamiltonian formulations; displacement-momentum and strain-momentum forms. Section 2 reintroduces the PDS-FEM formalism and derives the corresponding discretized Hamiltonian system for the two methods, and section 3 describes the time integration schemes. Section 4 presents the verification of the two methods with known solutions for a 1D and a 3D problem. Section 5 describes the validation of our method by comparison with photoelastic fringe patterns of a propagating crack, captured with a 1Mfps camera. Section 6 compares the two Hamiltonian formulations in term of numerical accuracy and computational efficiency. Section 7 presents some preliminary results of supershear rupture simulations using the above methods.

1. Two Hamiltonian formulations of elastic wave propagation

Lagrangian based formulations are often used in continuum mechanics to solve dynamic problems with FEM based numerical methods. Classically, the Lagrangian is written:

$$L(\boldsymbol{v},\boldsymbol{u}) = \int_V l(\boldsymbol{v},\boldsymbol{u})dV = \int_V \frac{1}{2}\rho \boldsymbol{v}^2 dV - \int_V \frac{1}{2}\boldsymbol{\nabla u}\colon \boldsymbol{C}\colon \boldsymbol{\nabla u}\, dV$$

According to the Hamilton's principle, the Euler-Lagrange equation can be derived as:

$$\frac{\partial \dot{l}}{\partial \boldsymbol{v}} = \frac{\partial l}{\partial \boldsymbol{u}}$$

By using a Legendre's transform:

$$l(\boldsymbol{v},\boldsymbol{u}) = \boldsymbol{p}.\boldsymbol{v} - h(\boldsymbol{p},\boldsymbol{u})$$

an alternative formulation using the Hamiltonian operator can be used based on the pair of variables momentum $\boldsymbol{p}$ and displacement $\boldsymbol{u}$, leading to the dynamic system:

$$\begin{cases} \dot{\boldsymbol{p}} = -\dfrac{\partial h}{\partial \boldsymbol{u}} \\ \dot{\boldsymbol{u}} = \dfrac{\partial h}{\partial \boldsymbol{p}} \end{cases} \quad (1)$$

where h is the Hamiltonian density.

An alternative is to use the strain $\boldsymbol{\epsilon}$ as a variable instead of the displacement. By doing so, the variable of interest for most mechanical problems, especially when fracture is involved, is directly computed through the formulation. This analytically equivalent system, when used for numerical computation, would reduce the number of floating point operations to obtain the strain/stress distribution, potentially leading to an improved accuracy. Considering the Lagrangian:

$$L(\boldsymbol{v},\boldsymbol{\epsilon}) = \int_V l(\boldsymbol{v},\boldsymbol{\epsilon})dV = \int_V \frac{1}{2}\rho \boldsymbol{v}^2 dV - \int_V \frac{1}{2}\boldsymbol{\epsilon}:\boldsymbol{C}:\boldsymbol{\epsilon}\, dV,$$

we can obtain the equivalent strain based Euler-Lagrange equation:

$$\frac{\partial \dot{l}}{\partial \boldsymbol{v}} = -\nabla.\frac{\partial l}{\partial \boldsymbol{\epsilon}},$$

from which we can directly derive the Hamiltonian system (see [11] for more details of the derivation):

$$\begin{cases} \dot{\boldsymbol{p}} = \nabla.\dfrac{\partial h}{\partial \boldsymbol{\epsilon}} \\ \dot{\boldsymbol{\epsilon}} = sym\left\{\nabla \dfrac{\partial h}{\partial \boldsymbol{p}}\right\} \end{cases} \qquad (2)$$

The set of equations (1) and (2) are the strong forms of the $(\boldsymbol{p},\boldsymbol{u})$ and $(\boldsymbol{p},\boldsymbol{\epsilon})$ based Hamiltonian formulations.

To numerically solve the above two Hamiltonian systems, we derive a discretized system in space and time, which is detailed in the two next sections.

2. Space discretization in PDS-FEM

2.1 Model and consistency condition

For the spatial discretization, we use a model of FEM based on Particle Discretization Scheme (PDS) as proposed in [7], due to its advantages in modeling cracks. PDS uses conjugate tessellations to approximate functions and their derivatives respectively. The Delaunay tessellation (indexed with β) is defined by a tetrahedron mesh, and the conjugate Voronoi tessellation (indexed with α), is constructed as indicated schematically in Fig. 1. In 2D, a Voronoi element or "particle" is essentially derived from joining the mass centers of the neighboring triangle elements.

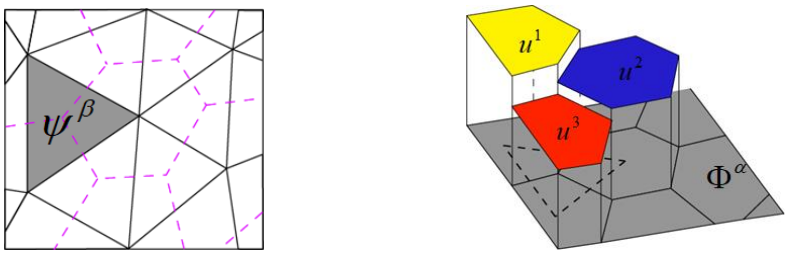

(a) Delaunay tessellation (b) Voronoi tessellation

Figure 1: Conjugate tessellations in 2D

In the model formulation, non-overlapping functions are used to approximate the functions and their derivatives respectively:

$$\boldsymbol{f}(\boldsymbol{x}) \approx \boldsymbol{f^d}(\boldsymbol{x}) = \sum_{\boldsymbol{\alpha=1}}^{\boldsymbol{N^\alpha}} \sum_{\boldsymbol{n=0}}^{\boldsymbol{|P^\alpha|}} \boldsymbol{f^{\alpha n}} P^{\alpha n}(\boldsymbol{x})\, \varphi^{\alpha}(\boldsymbol{x})$$

$$\boldsymbol{\nabla_{,i} f}(\boldsymbol{x}) \approx \boldsymbol{g^d}(\boldsymbol{x}) = \sum_{\boldsymbol{\beta=1}}^{\boldsymbol{N^\beta}} \sum_{\boldsymbol{m=0}}^{\boldsymbol{|Q^\beta|}} \boldsymbol{g_i^{\beta m}} Q^{\beta m}(\boldsymbol{x})\, \psi^{\beta}(\boldsymbol{x}),$$

where φ^{α} and ψ^{β} are respectively the characteristic functions of Voronoi and Delaunay elements. The displacement field is discretized on the Voronoi tessellation while the strain and stress distribution are discretized on the Delaunay tessellation.

PDS obtains bounded and consistent approximations for derivatives, $\boldsymbol{g}^d$, over the Delaunay tessellations by minimizing the following measure of error:

$$\min_{g^{\beta m}} \int_{\Psi^\beta} (\boldsymbol{g^d} - \nabla \boldsymbol{f^d})^2 dV$$

which leads to:

$$\boldsymbol{g}^{\beta m} = \boldsymbol{B}^{\beta \alpha m n} \otimes \boldsymbol{f}^{\alpha n}$$

With

$$B_i^{\beta \alpha m n} = \sum_{m'} \left(I^{\beta^{-1}}\right)^{m,m'} \int_V \frac{\partial (P^{\alpha n} \phi^{\alpha})}{\partial x_i} Q^{\beta m} \psi^{\beta} dV$$

$$I^{\beta m m'} = \int_{\Psi^\beta} Q^{\beta m} Q^{\beta m'} dV$$

The complete derivation of the vector $\boldsymbol{B}^{\beta \alpha m n}$ is provided in [10]. Then, applying it to the strain-displacement relationship, the consistency condition is written:

$$\boldsymbol{\epsilon}^{\beta m} = sym\{\boldsymbol{B}^{\beta \alpha m n} \otimes \boldsymbol{u}^{\alpha n}\} \qquad (3)$$

For the ease of computer implementation, we use the Voigt notation and express the above in matrix notation as follows:

$$\epsilon^{\beta m} = \tilde{B}^{\beta \alpha m n} . u^{\alpha n} \qquad (4)$$

2.2 Discretized Lagrangian and Hamiltonian forms

In this model, a discretized Lagrangian can be written $L(v^{\alpha n}, u^{\alpha n})$ or $L(v^{\alpha n}, \epsilon^{\beta m})$ depending on the formulation, and the corresponding Euler-Lagrange equations can be written as:

$$\frac{d}{dt}\frac{\partial L}{\partial v^{\alpha n}} = \frac{\partial L}{\partial u^{\alpha n}} \qquad \text{and} \qquad \frac{d}{dt}\frac{\partial L}{\partial v^{\alpha n}} - \sum_{\beta, m} {}^{t}\tilde{B}^{\beta \alpha m n} . \frac{\partial L}{\partial \epsilon^{\beta m}} = 0 \qquad (5)$$

By applying the Legendre transform:

$$L(v^{\alpha n}, u^{\alpha n}) = p^{\alpha n} . v^{\alpha n} - H(p^{\alpha n}, u^{\alpha n}) \qquad \text{or} \qquad L\left(v^{\alpha n}, \epsilon^{\beta m}\right) = p^{\alpha n} . v^{\alpha n} - H(p^{\alpha n}, \epsilon^{\beta m})$$

with

$$p^{\alpha n} = \frac{\partial L}{\partial v^{\alpha n}} = \rho \sum_{n'=0}^{|P^\alpha|} v^{\alpha n'} I^{\alpha n n'}, \qquad I^{\alpha n n'} = \int_{\Phi^\alpha} P^{\alpha n} P^{\alpha n'} dV, \tag{6}$$

we can obtain the following two equivalent Hamiltonian systems:

$$\begin{cases} \dot{p}^{\alpha n} = -\dfrac{\partial H}{\partial u^{\alpha n}} \\ \dot{u}^{\alpha n} = \dfrac{\partial H}{\partial p^{\alpha n}} \end{cases} \tag{7}$$

$$\begin{cases} \dot{p}^{\alpha n} = -\displaystyle\sum_{\beta}^{N^\beta} \sum_{m}^{|Q^\beta|} {}^t\tilde{B}^{\beta \alpha m n} . \frac{\partial H}{\partial \epsilon^{\beta m}} \\ \dot{\epsilon}^{\beta m} = \displaystyle\sum_{\alpha}^{N^\alpha} \sum_{n}^{|P^\alpha|} \tilde{B}^{\beta \alpha m n} . \frac{\partial H}{\partial p^{\alpha n}} \end{cases} \tag{8}$$

The derivation for the strain formulation is detailed in Appendix A.

2.3 Discretized Hamiltonian for continuum mechanics

Using the classical form of the Lagrangian in continuum mechanics (excluding for now the boundary conditions whose treatment is detailed in appendix B) and applying the Legendre's transform, we can write explicitly the Hamiltonian as:

$$H(p^{\alpha n}, u^{\alpha n}) = T(p^{\alpha n}) + U(u^{\alpha n})$$

Where, using Einstein's summation convention:

$$\begin{cases} T(p^{\alpha n}) = \dfrac{1}{2\rho} W^{\alpha n n'} \; {}^t p^{\alpha n} . p^{\alpha n'} \\ U(u^{\alpha n}) = \dfrac{1}{2} I^{\beta m m'} \; {}^t u^{\alpha n} . \; {}^t\tilde{B}^{\beta \alpha m n} . c^\beta . \tilde{B}^{\beta \alpha' m' n'} . u^{\alpha' n'} \end{cases}$$

with

$$W^\alpha = I^{\alpha^{-1}}$$

Similarly, the Hamiltonian can be written in term of strain:

$$H\left(p^{\alpha n}, \epsilon^{\beta m}\right) = T(p^{\alpha n}) + U(\epsilon^{\beta m})$$

where

$$U\left(\epsilon^{\beta m}\right) = \frac{1}{2} I^{\beta m m'} \; {}^t\epsilon^{\beta m} . c^\beta . \epsilon^{\beta m'}$$

We can then replace the Hamiltonian derivatives in the Eq. 7 and 8 to obtain the Hamiltonian systems in displacement-momentum form as:

$$\begin{cases} \dot{p}^{\alpha n} = -\displaystyle\sum_{\alpha'}^{N^\alpha} \sum_{n'}^{|P^\alpha|} K^{\alpha n \alpha' n'} . u^{\alpha' n'} \\ \dot{u}^{\alpha n} = \dfrac{1}{\rho} \displaystyle\sum_{n'}^{|P^\alpha|} W^{\alpha n n'} . p^{\alpha n'} \end{cases}, \tag{9}$$

where

$$K^{\alpha n \alpha' n'} = \sum_{\beta}^{N^{\beta}} \sum_{m,m'}^{|Q^{\beta}|} I^{\beta m m'} \; {}^{t}\tilde{B}^{\beta \alpha m n} . c^{\beta} . \tilde{B}^{\beta \alpha' m' n'},$$

and in strain-momentum form as:

$$\begin{cases} \dot{p}^{\alpha n} = -\sum_{\beta}^{N^{\beta}} \sum_{m,m'}^{|Q^{\beta}|} I^{\beta m m'} \; {}^{t}\tilde{B}^{\beta \alpha m n} . c^{\beta} . \epsilon^{\beta m'} \\ \dot{\epsilon}^{\beta m} = \sum_{\alpha}^{N^{\alpha}} \sum_{n,n'}^{|P^{\alpha}|} \frac{1}{\rho} W^{\alpha n n'} \tilde{B}^{\beta \alpha m n} . p^{\alpha n'} \end{cases} . \qquad (10)$$

2.4 Crack treatment

The above derived system of governing equations is valid for time invariant topologies, and some adaptations are necessary to simulate dynamic crack propagation. As shown in Fig. 1b, the displacement approximated with PDS is discontinuous at the Voronoi boundaries, $\partial\Phi^{\alpha}$. PDS uses these discontinuities to model a crack propagating along a Voronoi boundary by nullifying appropriate mechanical contributions. In the 3D case, each tetrahedral Delaunay element contains 6 Voronoi surfaces along which the cracks can appear (see Fig. 2).

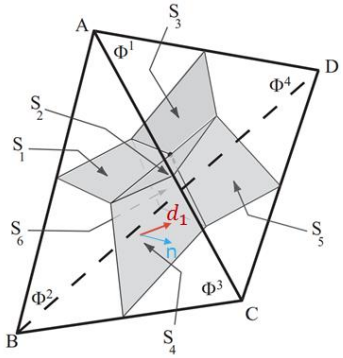

Figure 2: Surfaces of interaction

If the maximum principle stress is greater than a given value σ_s, the surface whose normal n is closer to the principal stress direction d_1 (corresponding to the surface with highest tensile stress) is broken, nullifying its contribution to the strain ϵ^{β}, by modifying the coefficient $B_i^{\beta \alpha m n}$:

$$\int_V \frac{\partial (P^{\alpha n} \phi^{\alpha})}{\partial x_i} Q^{\beta m} \psi^{\beta} dV = \int_{\Psi^{\beta} \cap \Phi^{\alpha}} \frac{\partial P^{\alpha n}}{\partial x_i} Q^{\beta m} dV + \int_{\Psi^{\beta} \cap \partial\Phi^{\alpha} - s} P^{\alpha n} Q^{\beta m} n_i \, dV + \underbrace{\int_s P^{\alpha n} Q^{\beta m} n_i \, dV}_{\to 0}$$

The first right-hand term corresponds to the volume component of the gradient (null for rigid particles with constant displacement, unchanged by the crack). The second and third right-hand terms correspond to the surface component coming from the interaction between the particles, for the unbroken and broken surfaces respectively. The latter contribution is set to zero.

For the sake of simplicity, the maximum principal stress criterion is used for the simulations presented in this paper. However, at the crack tip, larger elements have a lower average stress value and so are less prone to crack, making this criterion mesh dependent, although it doesn't affect the crack path as long as the crack prone region is homogeneously refined.

3. Time integration schemes

Out of the large collection of algorithms for the time integration of Hamiltonian systems, we chose to use the Störmer-Verlet integration scheme, which is a second order variational integrator (see for instance [22] section VI for reference):

$$\begin{cases} p_{n+1/2} = p_n - \dfrac{dt}{2}\dfrac{\partial H}{\partial u}(p_{n+1/2}, u_n) \\ u_{n+1} = u_n + \dfrac{dt}{2}\left(\dfrac{\partial H}{\partial p}(p_{n+1/2}, u_n) + \dfrac{\partial H}{\partial p}(p_{n+1/2}, u_{n+1})\right) \\ p_{n+1} = p_{n+1/2} - \dfrac{dt}{2}\dfrac{\partial H}{\partial u}(p_{n+1/2}, u_{n+1}) \end{cases}$$

In particular, the symplectic property of the flow (p, u) in time is ensured, which can be written:

$$\left(\frac{\partial\,(p_{n+1}, u_{n+1})}{\partial\,(p_0, u_0)}\right)^T J \left(\frac{\partial\,(p_{n+1}, u_{n+1})}{\partial\,(p_0, u_0)}\right) = J = \begin{pmatrix} 0 & I \\ -I & 0 \end{pmatrix},$$

where *I* is the identity matrix.

For the strain formulation, such symplectic property cannot be defined directly as the strain (dimension 6) and the momentum (dimension 3) don't belong to the same vector spaces. However, it is possible to express the above symplectic property in term of the strain and momentum variables. Using Eq. 4, we can write:

$$\frac{\partial \epsilon}{\partial u'} = \tilde{B} \qquad \text{and} \qquad \frac{\partial u'}{\partial \epsilon} = \tilde{B}^{-1},$$

with u' the displacement field excluding the Dirichlet boundary conditions and $\tilde{B}$ the corresponding reduced matrix built with the blocks $\tilde{B}^{\beta\alpha}$. $\tilde{B}^{-1}$ is the left inverse of $\tilde{B}$. If ϕ is the flow of the Hamiltonian system in (p, u) and ψ the flow of the Hamiltonian system in (p, ϵ), we can write

$$\frac{\partial \phi}{\partial (p_0, u_0)} = \underbrace{\begin{pmatrix} I_{3N^\alpha} & 0 \\ 0 & \tilde{B}^{-1} \end{pmatrix}}_{A^{-1}} \frac{\partial \psi}{\partial (p_0, \epsilon_0)} \underbrace{\begin{pmatrix} I_{3N^\alpha} & 0 \\ 0 & \tilde{B} \end{pmatrix}}_{A}.$$

Therefore, we can express the symplectic property from the flow ψ:

$$\left(A^{-1}\frac{\partial \psi}{\partial (p_0, \epsilon_0)}A\right) J \left(A^{-1}\frac{\partial \psi}{\partial (p_0, \epsilon_0)}A\right) = J$$

Following this property, we can derive an algorithm equivalent to the classical Störmer-Vertlet scheme for (p, ϵ) (Einstein convention is used for the summation):

$$\begin{cases} p_{n+1/2} = p_n - \dfrac{dt}{2}\ {}^t\tilde{B}.\dfrac{\partial H}{\partial \epsilon}(p_{n+1/2}, \epsilon_n) \\ \epsilon_{n+1} = \epsilon_n + \dfrac{dt}{2}\tilde{B}.\left(\dfrac{\partial H}{\partial p}(p_{n+1/2}, \epsilon_n) + \dfrac{\partial H}{\partial p^\alpha}(p_{n+1/2}, \epsilon_{n+1})\right) \\ p_{n+1} = p_{n+1/2} - \dfrac{dt}{2}\ {}^t\tilde{B}\dfrac{\partial H}{\partial \epsilon}(p_{n+1/2}, \epsilon_{n+1}) \end{cases}$$

By ensuring the conservation of the momentum, the average conservation of the total energy, and the symplecticity of the two systems, these time integration schemes can maintain accuracy and stability in long-time integration.

Since our Hamiltonians are separable, the integration scheme computation becomes explicit (see Eq. 9 and 10). In particular, the time integration scheme can be written in the matrix form as:

$$\begin{cases} \boldsymbol{p_{n+1/2} = p_n - \frac{dt}{2} K_1 q_n} \\ \boldsymbol{q_{n+1} = q_n + dt\, K_2 p_{n+1/2}} \\ \boldsymbol{p_{n+1} = p_{n+1/2} - \frac{dt}{2} K_1 q_{n+1}} \end{cases}$$

where $\boldsymbol{q_n}$ represents either $\boldsymbol{u_n}$ or $\boldsymbol{\epsilon_n}$, and $\boldsymbol{K_1}$, $\boldsymbol{K_2}$ are two matrices derived from the expanded Hamiltonian form.

4. Verification of dynamic crack propagation simulations

In order to verify the application of above schemes to simulate dynamic crack propagation simulations, we compare the results of the simulation with the known solutions of a 1D spallation problem and a 3D torsion problem.

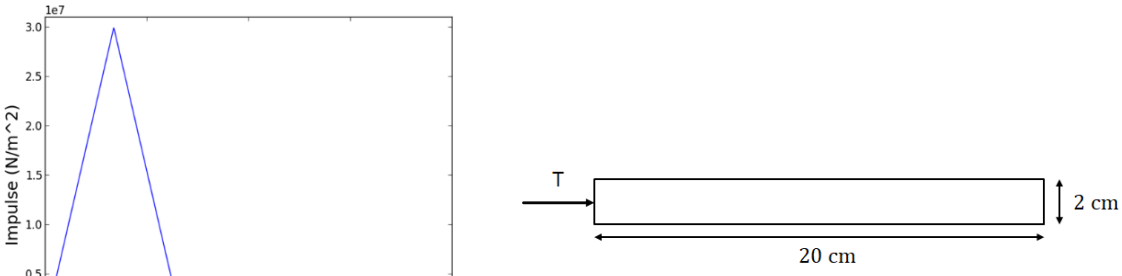

(a) Impulse shape (b) Geometrical setting

Figure 3: Problem settings for the spallation test

4.1 1D spallation problem

One mode of material failure during high velocity impact is spallation. As an example, an impact on one end of a bar creates a compressive wave which is then inverted and reflected at the opposite end, resulting in a high tensile stress wave likely to generate a crack. In this verification test, we consider the problem settings shown in Fig. 3, and compare the position of the crack and the time of occurrence with the corresponding analytical solution. We chose a simple stress criterion with the strength $\sigma_c = 29.5$MPa, slightly lower than the amplitude of the input wave as we observe a small loss of amplitude with the propagation. Obviously the crack opens when the tensile stress, propagating backwards after reflection on the right tip, exceeds this limit value. It can be shown that the maximum tensile stress occurs at $t = L/c + 3T/4 = 1.65\ 10^{-4}s$ and $x = L - cT/4 = 0.171\ m$ where $L = 0.2m$ is the length of the bar, $c = 1.75\ 10^{-3}m.s^{-1}$ the wave velocity and $T = 6.7\ 10^{-5}s$ the impulse duration. The numerical simulations produced the crack at the above theoretically expected time and location (see Fig. 4), with reasonably small errors of $\pm\ 5.0 \times 10^{-7}s$ and $-\ 1.0 \times 10^{-3}$m, respectively.

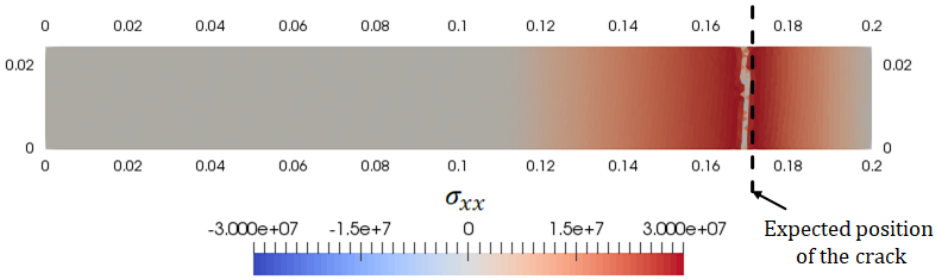

Figure 4: Simulated crack position and stress distribution for spallation

4.2 Torsional cracks in a cylindrical specimen

To verify that the above schemes can reproduce the 3D geometry of dynamically growing cracks, we consider the classical experiment of torsion of a cylinder bar with the standard dimensions (in mm, see Fig. 5) and the following material properties:

- Young Modulus: 3.0 GPa
- Tensile strength: 30 MPa
- Density: 1.25 kg.m^{-3}

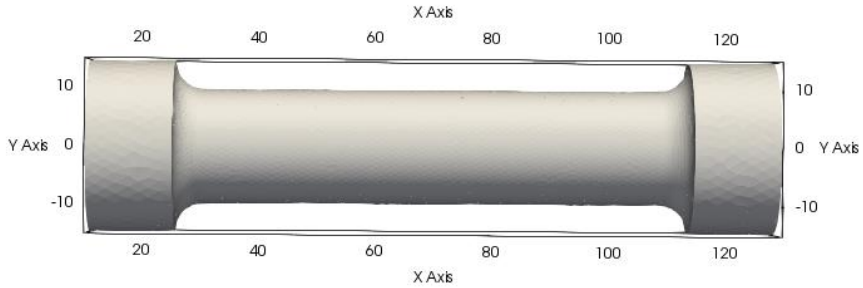

Figure 5: Geometrical setting for the torsion simulation

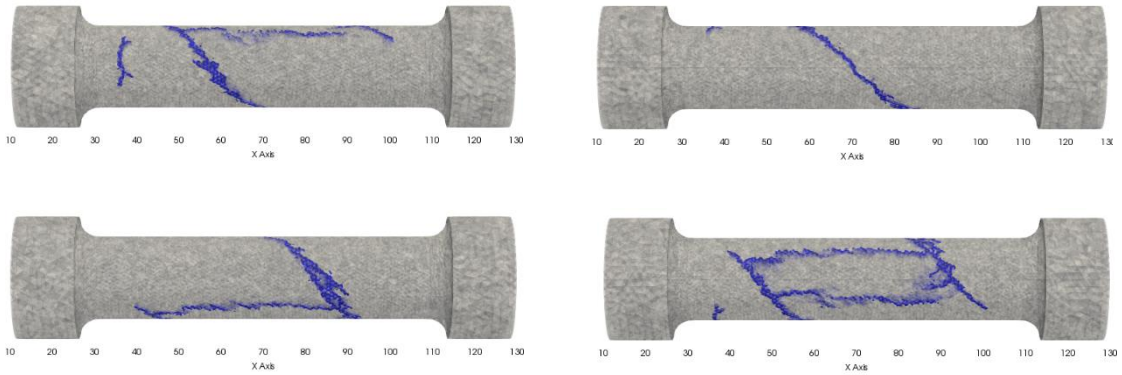

Figure 6: Trace of the crack on the surface from 4 different angles

The right end of the bar ($x \geq 115mm$) is fixed at all time (i.e. $p = 0$), while the left end of the bar ($x \leq 25m$) is rotated at the angular speed $\dot{\theta} = 3° \, s^{-1}$. In order to save computation time, we first solve the static problem for a rotation of angle $\theta = 6.3°$, which brings the principal stress on the surface very close to the tensile strength, and then proceed to the dynamic loading. In this problem, anywhere on the surface of the cylinder is primed to crack, as the shear stress is uniformly distributed. So as to control where the crack will initiate, in particular to avoid having a crack propagating near the two extremities, we generate a small initial crack on the surface near the middle of the bar. The trace of the crack on the surface after completed fracture is shown in Fig. 6.

Though we lack experimental observations of the crack propagation speed, we observe that the crack begin to open at the expected load, and that the total crack path corresponds to the classical spiral shape oriented at 45° observed during torsion test, albeit a few branches. Additional experimental measures of secondary crack patterns inside ruptured material would be needed to verify this observation.

5. Validation

5.1 Experimental setting

The PDS-FEM implementations for dynamic crack propagation simulations are validated by comparing with high speed photoelastic observations of a dynamic mode-I crack captured with a 1Mfps camera. These photoelastic fringes characterize the stress distribution in the material, specifically the difference between the two principal stresses. The experimental setting is shown in Fig. 7, and the Epoxy resin (CY232 & HY951) sample has the following properties:

- Young modulus: 3.84 GPa
- Poisson ratio: 0.3
- Static photoelastic constant: 0.53 mm/N (measured by calibration with a Brazilian test)

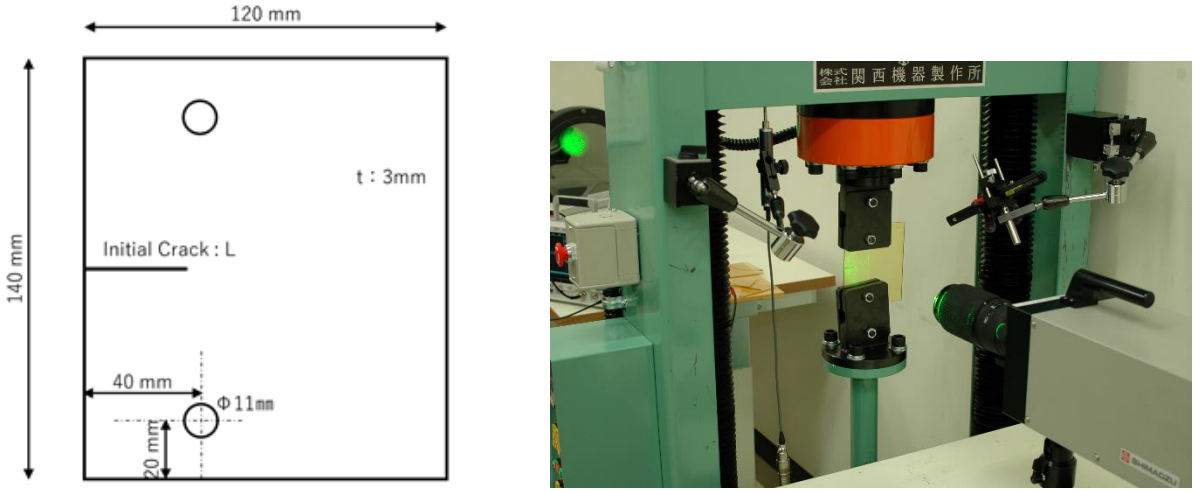

(a) Geometry of the sample (b) Experimental setting without analyzer

Figure 7: Experimental setting

Two bars are inserted in the holes of the plate, and then respectively pulled up and down. The pulling phase is displacement controlled, and the corresponding applied force loading is also measured. In the experiment conducted, the initial crack was 1 mm wide, and 20.5 mm long. The displacement is increased at a speed of 0.5 mm/min until the onset of crack propagation. Compared to the few hundred μs period required for the crack to move across the sample, our external loading can be considered quasi-static and the positions of the bars fixed during the duration of the propagation. As the initial displacement required to bring the bars and the holes just in contact cannot be accurately estimated from the available experimental observations, we use the equivalent force load in our simulations. In the experiment, the crack initiated at 0.54 kN. The same load is used to calculate the static solution before the crack initiation, which will be used as the initial condition of the dynamic problem. The stress criterion for rupture is chosen to be the maximum value for which the crack propagates in the simulation (corresponding to 40 MPa for tetrahedral elements of average size 0.2 mm). We used 0^{th} order PDS-FEM discretization, which corresponds to constant values of the variables in each element.

5.2 Numerical model

In order to accurately reproduce the crack tip stress field, we refined the mesh as follows (also, see Fig. 8):

- Most outer elements ($|y - 0.07| > 0.01$ or $z > 0.045$): average size 1 mm.
- Intermediate layer ($0.005 < |y-0.07| < 0.01$): average size 0.5 mm, refinement required for the observation of the fringe patterns, but not very fast variation of stress
- Inner band ($|y - 0.07| < 0.005$): average size of 0.2 mm, refinement required to capture well the stress distribution around the crack tip, all along its propagation.

In total, the mesh consists of around 3×10^6 elements and 5×10^5 nodes. 288 MPI processes are used for the computation.

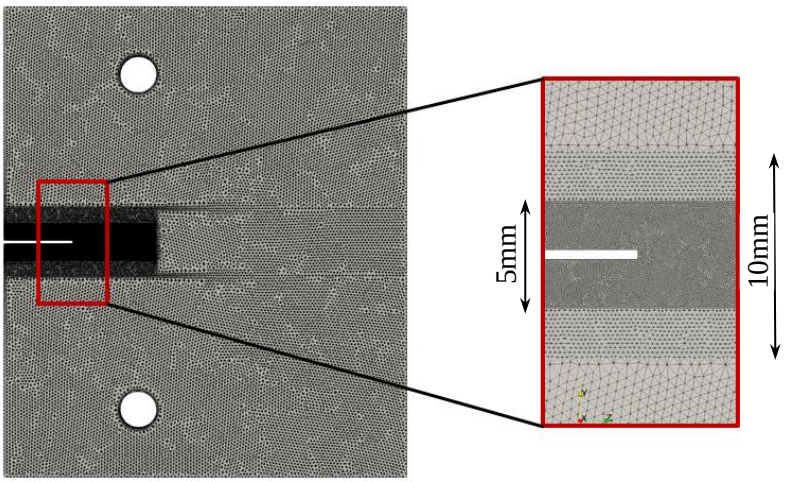

Figure 8: Mesh refinement

5.3 Observations

Crack path

The horizontal crack path observed in the experiment is correctly reproduced in the simulation.

Stress distribution

The propagation of the crack and the fringe patterns are captured with a high speed camera, with a capturing speed of 1Mfps. Figure 9 compares the observed fringe patterns with those corresponding to the crack propagation simulation; (p, ϵ) form is used.

Fringe patterns, which characterize the difference of principal stresses in the material, are very sensitive to the change of stress distribution. In this experiment, each fringe corresponds to an increment of 3.95 MPa of the principal stresses difference. As seen in Fig. 9, the numerical results are in good agreement with those observed in the experiment. In particular, the amplitude of the main fringes decreases the same amount (the fringes get closer to the crack tip) when the propagation begins.

In the simulation results, we can clearly observe a wave emanating from the moving crack, which is completely absent in the experimental observations. This is most likely due to our failure criterion. As the stress is considered constant inside an element, a surface rupture releases a relatively high amount of energy (corresponding to the strain energy of the entire element), creating a source point for a stress wave, whose amplitude might decrease with a more refined mesh (for which the rupture is more "continuous"). This wave could also be smoothened if higher order functions are considered and the stress release limited to the zone

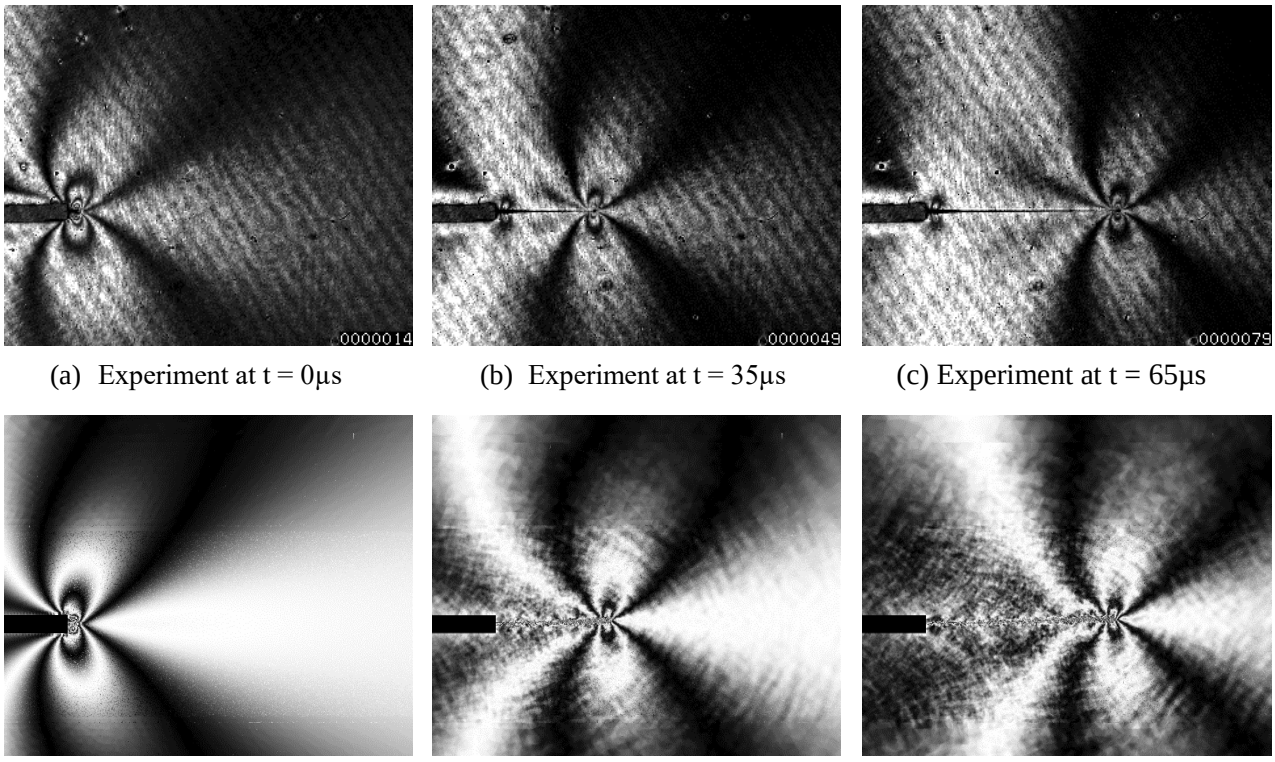

(a) Experiment at t = 0μs (b) Experiment at t = 35μs (c) Experiment at t = 65μs

(d) Simulation at t = 0μs (e) Simulation at t = 35μs (f) Simulation at t = 65μs

Figure 9: Comparison of the fringe patterns at three stages; (a)-(c) are experimental while (d)-(f) are numerical. Each fringe corresponds to an increase of 3.95 MPa

surrounding the surface. Also, the camera recording might have a smoothing effect as the assumed wave propagates between two frames and only its average value can be recorded.

Crack propagation speed

For $t \leq 20\ \mu s$, the propagation speed in the simulation is almost twice faster than in the experiment. For $t > 20\ \mu s$, the crack tip position in the simulation is about $5\ \mu s$ ahead of the crack tip position measured in the experiment until $t = 60\ \mu s$, after which the position of the crack in both the simulation and the experiment are in fairly good agreement, showing that the average speed of the simulated crack is consistent with the experiment. The record of crack tip position is detailed in table 1.

Table 1: Comparison of the crack tip position

Time [μs]	0	10	20	30	40	50	60	70	80
Experiment [mm]	0.5	1.6	3.0	4.6	6.2	7.8	9.6	11.3	13.5
Simulation [mm]	0.6	3.3	4.9	5.9	7.0	8.6	9.6	11.3	13.3

6. Comparison of the two formulations

Although the strain-based formulation and the displacement-based formulation presented in sections 2 and 3 are analytically equivalent, they lead to different numerical schemes. Therefore, they may produce stress and displacement distributions with different degrees of accuracy. In particular, in the strain formulation, the strain is computed directly by the dynamic system, though additional calculations are required to extract the displacement distribution. Therefore,

it is expected that the strain formulation would be more accurate for the stress distribution while the displacement formulation would be more accurate for the displacement distribution.

In this section, we compare quantitatively computational efficiency and numerical accuracy of these two formulations. For this comparison, we use the dynamic crack propagation problem presented in the section 5. Since this problem is very sensitive to changes in the stress/displacement distribution which could particularly alter the direction and the speed of the crack, it is an ideal problem to identify potential numerical differences. Figure 10 shows the maximal magnitude of the difference between stress distributions in the whole sample along time.

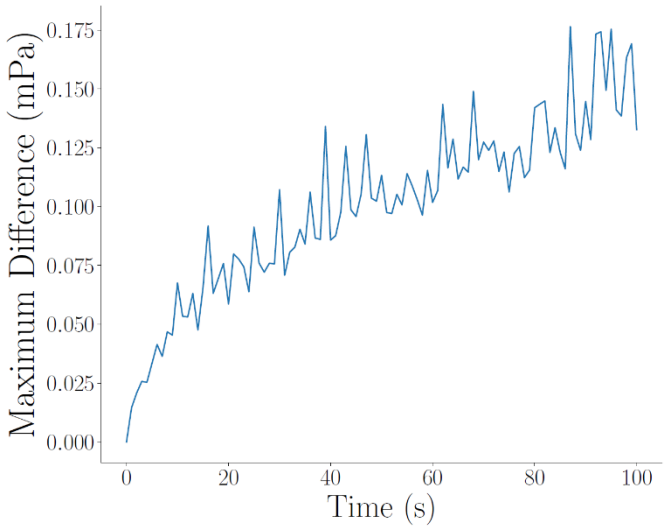

Figure 10: Comparison of the stress distribution between the two formulations

We observe that the maximum difference, although increasing with time, remains very insignificant compared to the relevant level of stress in the sample (order of a few MPa). Similar results can be observed for the displacement formulation although we don't show it in this article. Therefore, on a numerical accuracy perspective, both formulations can be considered equivalent.

On a computational perspective, however, there is a significant difference. The main computational task in the respective dynamic systems are the matrix-vector multiplications. However, as the mesh contains significantly more tetrahedron elements than nodes, and that strain vectors have at least 6 components while displacement only have 3 components, it is clear that strain formulation involves much more floating point operation in the main computation. Also, additional overhead is required to compute the strain change due to the rupture of an element in the strain formulation. The memory usage and average computation time for a single iteration are compared in Table 2. In order to avoid additional overheads related to parallel computing, like communication time, the compared values are obtained from one of the MPI process (with 2×10^4 elments and 4×10^3 nodes), out of the 288 MPI processes used for the computation.

Table 2: Comparison of computational performance

	Disp formulation	Strain Formulation
Single process memory usage (MB)	6.1	14.8 (+35.3 crack strain overhead)
Single iteration simulation time (s)	0.0304	0.0857

We observe that the strain formulation is significantly more computationally demanding, both in memory usage and computation time. Further, as shown above, both formulations essentially lead to a near identical numerical accuracy. Therefore, we conclude that it is more relevant to use the displacement formulation in general.

7. Application to supershear rupture simulation

7.1 Theoretical considerations

In this section, we apply the developed numerical method to the simulation of an idealized supershear rupture in earthquakes. This part should be understood as an illustration of the potential capabilities of this method rather than a full study of supershear rupture.

Supershear rupture is defined as a crack propagation faster than the S-wave velocity, producing a characteristic shear wave Mach cone following the crack tip. The possible occurrence of this kind of rupture was first theoretically predicted by Burridge *et al.*[12], who identified three steady crack propagation regimes:

- $v_r < c_R$: sub Rayleigh regime
- $c_s < v_r < \sqrt{2}c_s$: unstable intersonic (supershear) rupture
- $\sqrt{2}c_s < v_r < c_P$: stable intersonic (supershear) rupture

The zone $c_R < v_r < c_s$ is forbidden as it leads to a negative fracture energy.

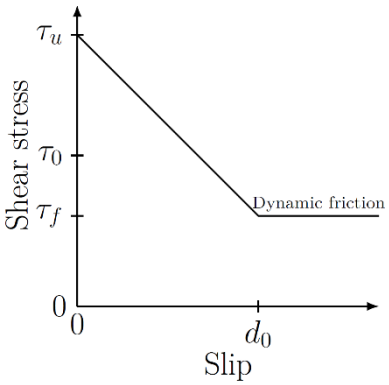

Figure 11: Linear Slip-weakening law

In the case of earthquakes, fault "rupture" corresponds to the part of the fault where slipping occurs, where there is a discontinuity of displacement across the fault. For the slipping, the linear slip-weakening friction law used by Andrews [13], shown in Fig. 11, is a good first approximation of the earthquake slipping law, and has been widely used for the simulation of supershear rupture. The initial stress in the material is noted τ_0. When a perturbation makes the stress exceed the maximum cohesive strength τ_u (static frictional stress), slipping starts and the maximum frictional stress decreases linearly until a minimum τ_f corresponding to the dynamic frictional stress.

Although diverse factors, like fault roughness, local material heterogeneities, asperities etc., can influence the occurrence of supershear rupture, for the ideal scenario of a perfectly straight plane fault in an otherwise homogenous material, the seismic factor, introduced by Das and Aki [14]:

$$s = \frac{\tau_u - \tau_0}{\tau_0 - \tau_f}$$

characterizes the crack propagation regimes. In particular, for a 2D problem, supershear propagation is theoretically possible only for $s < 1.77$ [13]. In our simulation, we don't

observe supershear rupture for $s \geq 1.1$, which might be partly due to wave defocusing in 3D plates compared to an actual 2D setting.

7.2 Numerical problem setting

We simulate the rupture in a crust layer of dimensions $10\ km \times 4\ km\ \times\ 0.1\ km$, centered around a fault plane extending all along the layer (see Fig. 12). The parameters for the slip weakening law are chosen arbitrarily, which is sufficient for this qualitative study, as they influence only the slip-weakening zone length and the seismic factor. We use the following material properties corresponding to the Earth crust:

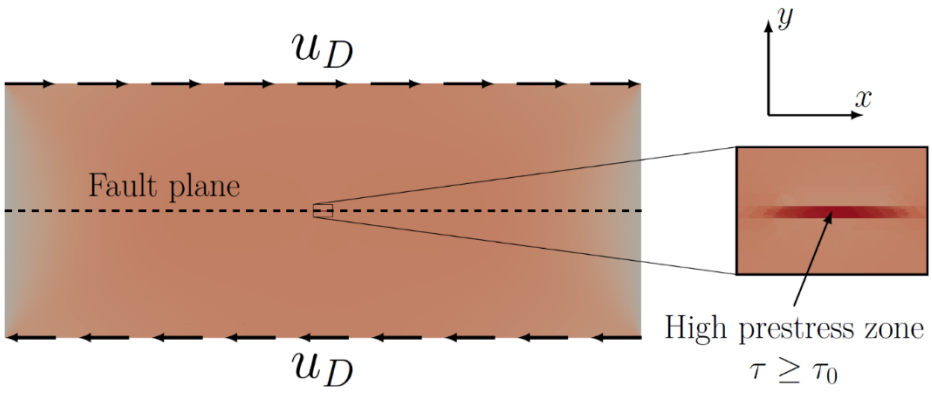

Figure 12: Supershear problem setting

- Young modulus: 75 GPa
- Poisson ratio: 0.3
- Density: 2.5 10^3 kg.m^{-3}
- $\tau_u = 100MPa$, $\tau_f = 0MPa$
- $d_0 = 0.2\ m$
- $\tau_0 = 44\ MPa$ $(s = 1.27)$ for sub-Rayleigh, $\tau_0 = 58\ MPa$ $(s = 0.7)$ for supershear

The corresponding P-wave and S-wave velocities are, respectively, $c_p = 5477m.s^{-1}$ and $c_S = 3162m.s^{-1}$.

At $t = 0$, the fault is perfectly cohesive and the stress/displacement is continuous across the fault (no broken element on the fault). We solve a static problem with Dirichlet boundary conditions to obtain the initial stress distribution. The fault parallel component u_D is fixed and the two other components are set to 0 on the Dirichlet boundaries.

At $t > 0$, if the stress exceeds the maximum shear stress in an element, the inner fault surface is broken and frictional forces are mobilized and distributed on the nodes on the fault surfaces, according to the slip-weakening friction law.

7.3 Results and observations

Stress and velocity distributions at $t = 0.4s$ on the surface for sub-Rayleigh and supershear regimes are shown in Fig. 13.

In the sub-Rayleigh scenario, we observe the classical wave pattern, with a clear S-wave front progressing ahead of the crack which propagates at c_R. The P-wave front is however not clearly observable. In the supershear scenario, we can clearly observe the P-wave front which is just ahead of the crack which propagates at a speed close to c_P. The Mach cone, characteristic of a shock wave propagation, is also clearly visible. Fault parallel velocity is significantly higher in

the supershear case, especially far from the fault. On the contrary, fault-normal velocity is higher for the sub-Rayleigh case near the crack tip, and dissipates rapidly far from the fault.

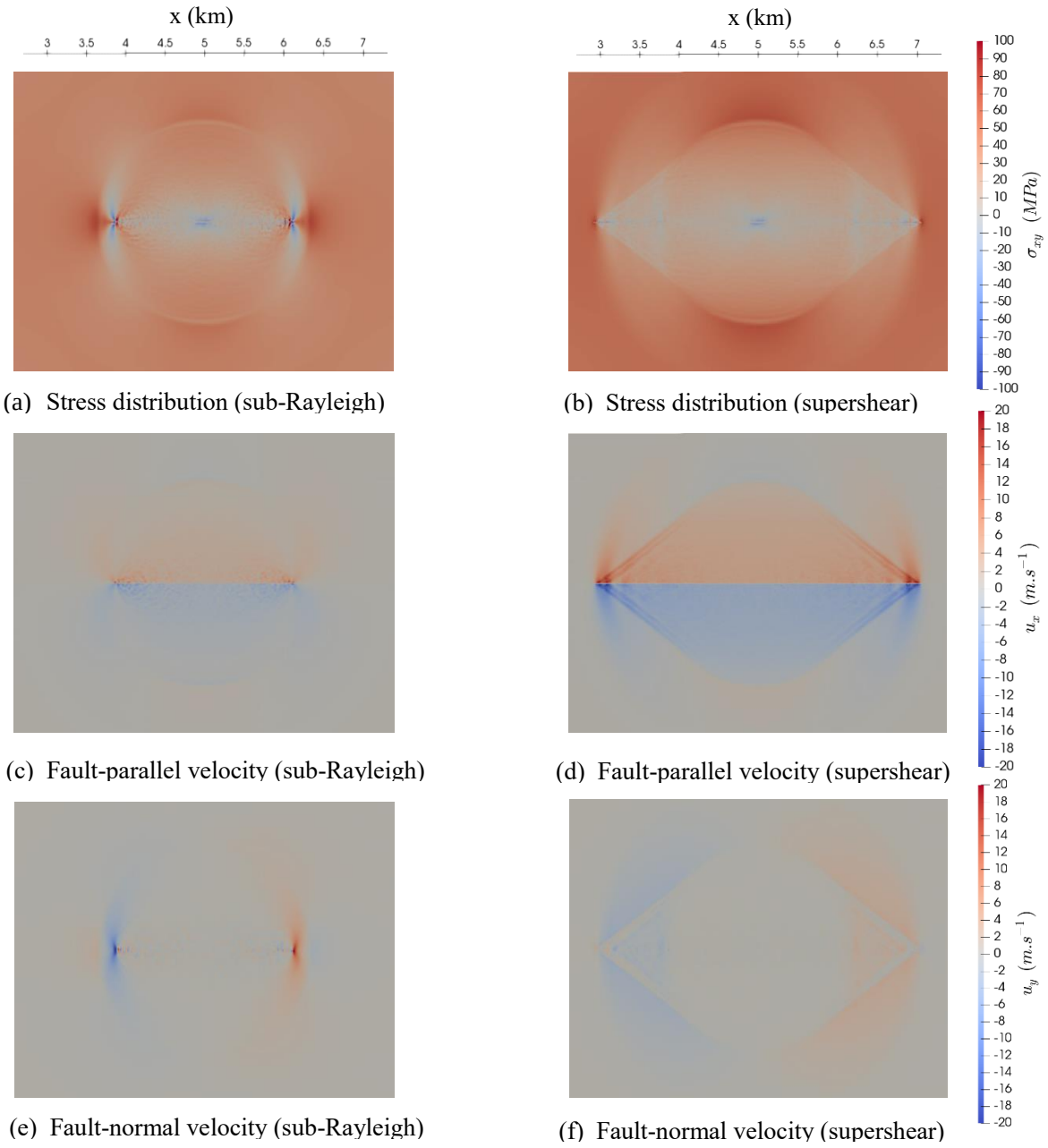

(a) Stress distribution (sub-Rayleigh)

(b) Stress distribution (supershear)

(c) Fault-parallel velocity (sub-Rayleigh)

(d) Fault-parallel velocity (supershear)

(e) Fault-normal velocity (sub-Rayleigh)

(f) Fault-normal velocity (supershear)

Figure 13: Stress and velocity distributions for sub-Rayleigh and supershear rupture at t=0.4s

7.4 Transition phenomenon

In the supershear rupture scenario, the rupture doesn't propagate immediately at intersonic speed. This transition from the initial sub-Rayleigh propagation to supershear rupture, in a homogenous material, is classically explained by the Burridge-Andrews mechanism [13]. At first, the crack propagate behind the shear wave, at a speed close to c_R. The P-wave and S-wave propagating ahead generate a zone of high shear stress ahead of the crack tip, eventually creating a secondary crack, also called daughter crack, if the prestress is sufficiently high. When the main crack merges with the daughter crack, there is a jump of the rupture velocity, thereby

starting the intersonic propagation. This phenomenon can be observed in our simulation, and is detailed in Fig. 14.

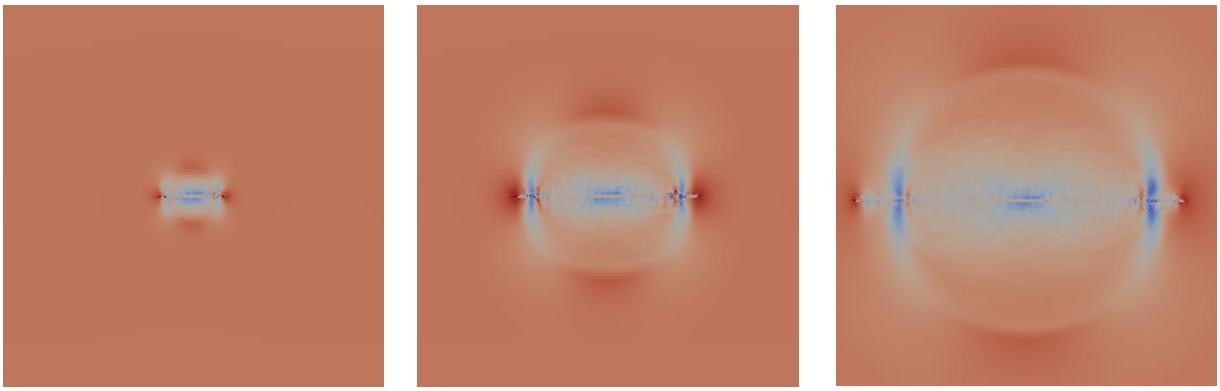

(a) Sub-Rayleigh propagation ($t = 0.05s$)

(b) Apparition of daughter crack ($t = 0.1s$)

(c) Transition to supershear rupture ($t = 0.25s$)

Figure 14: Burridge-Andrews mechanism observed in the simulation

Concluding remarks

We developed two Hamiltonian-based formulations in the frame of PDS-FEM, and derived consistent time integration schemes which are momentum conserving and symplectic. The separable nature of the Hamiltonian in continuum mechanics ensures that the computation can be done explicitly and thus is relatively cheap computationally. The results of the two verification tests and the validation test show a good accordance with the analytical solution when available, and with the experimental measures in term of crack path, propagation speed and stress distribution around the propagating crack tip. The results also showed that both formulations are numerically indifferentiable, although the displacement formulation proves to have a significantly lower computational cost. This paper also demonstrates that this numerical method can be applied to the simulation of supershear earthquakes, and that characteristic wave profiles and transition mechanism were qualitatively reproduced for both sub-Rayleigh and supershear fault rupture. We are improving computational capabilities of a parallel program with the aim of conducting large scale simulation of supershear earthquake scenarios with the models of actual faults.

Appendix A: Euler-Lagrange equation of the strain formulation

For the sake of simplicity, the indexes *m* and *n* defining the functions used for interpolation are omitted in the following derivation of the Hamilton's principle, as their inclusion is straightforward. Einstein summation is assumed in the following.
By using the Hamilton's principle, and using Eq. 3:

$$
\begin{aligned}
0 = \delta\left(\int_T L\left(\boldsymbol{v}^{\boldsymbol{\alpha}}, \boldsymbol{\epsilon}^{\boldsymbol{\beta}}\right) dt\right) &= \int_T \left(\frac{\partial L}{\partial \boldsymbol{v}^{\boldsymbol{\alpha}}} \cdot \boldsymbol{\delta \dot{u}}^{\boldsymbol{\alpha}} + \frac{\partial L}{\partial \boldsymbol{\epsilon}^{\boldsymbol{\beta}}} : \boldsymbol{\delta \epsilon}^{\boldsymbol{\beta}}\right) dt \\
&= \int_T \left(-\frac{\partial \dot{L}}{\partial \boldsymbol{v}^{\boldsymbol{\alpha}}} \cdot \boldsymbol{\delta u}^{\boldsymbol{\alpha}} + \frac{\partial L}{\partial \boldsymbol{\epsilon}^{\boldsymbol{\beta}}} : sym\{\boldsymbol{B}^{\boldsymbol{\beta\alpha}} \otimes \boldsymbol{\delta u}^{\boldsymbol{\alpha}}\}\right) dt \\
&= \int_T \left(-\frac{\partial \dot{L}}{\partial \boldsymbol{v}^{\boldsymbol{\alpha}}} \cdot \boldsymbol{\delta u}^{\boldsymbol{\alpha}} + \frac{\partial L}{\partial \epsilon_{ij}^{\beta}} B_i^{\beta\alpha} \delta u_j^{\alpha}\right) dt \\
&= \int_T \left(-\frac{\partial \dot{L}}{\partial \boldsymbol{v}^{\boldsymbol{\alpha}}} \cdot \boldsymbol{\delta u}^{\boldsymbol{\alpha}} + \frac{\partial L}{\partial \boldsymbol{\epsilon}^{\boldsymbol{\beta}}} \boldsymbol{B}^{\boldsymbol{\beta\alpha}} \cdot \boldsymbol{\delta u}^{\boldsymbol{\alpha}}\right) dt
\end{aligned}
$$

Note that only one integration by part is needed, instead of the two needed for the general analytical expression.

By writing $\frac{\partial L}{\partial \boldsymbol{\epsilon^{\beta}}}$ in vector form following Voigt notations: $\left(\frac{\partial L}{\partial \epsilon_{11}^{\beta}}, \frac{\partial L}{\partial \epsilon_{22}^{\beta}}, \frac{\partial L}{\partial \epsilon_{33}^{\beta}}, \frac{\partial L}{\partial \epsilon_{23}^{\beta}}, \frac{\partial L}{\partial \epsilon_{13}^{\beta}}, \frac{\partial L}{\partial \epsilon_{12}^{\beta}}\right)$, and rewriting $\boldsymbol{B^{\beta\alpha}}$ in the adapted matrix form:

$$ {}^{t}\tilde{B}^{\beta\alpha} = \begin{pmatrix} B_1^{\beta\alpha} & 0 & 0 & 0 & B_3^{\beta\alpha} & B_2^{\beta\alpha} \\ 0 & B_2^{\beta\alpha} & 0 & B_3^{\beta\alpha} & 0 & B_1^{\beta\alpha} \\ 0 & 0 & B_3^{\beta\alpha} & B_2^{\beta\alpha} & B_1^{\beta\alpha} & 0 \end{pmatrix} $$

and finally replacing them in the above integral, the vector form Euler-Lagrange equation (Eq. 5) can be derived.

Appendix B: Boundary conditions

Dirichlet BC

Let u_D be the value of displacement imposed on the boundary.
We will set the coefficients $u^{\alpha n}$ such as:

$$ \frac{\partial}{\partial u^{\alpha n}} \int_{\Gamma_D} \left| P^{\alpha' n'} u^{\alpha' n'} - u_D \right|^2 ds = 0 \Rightarrow \sum_{n'} I_S^{\alpha n n'} u^{\alpha n'} = \int_{\Gamma_D} u_D p^{\alpha n} \, ds $$

where $I_S^{\alpha n n'} = \int_{\Gamma_D} P^{\alpha n} P^{\alpha n'} ds$.

We note $W_S^{\alpha} = (I_S^{\alpha})^{-1}$, $u^{\alpha n} = \sum_{n'} W_S^{\alpha n n'} \int_{\Gamma_D} u_D p^{\alpha n'} \, ds$

This inverse is ensured to exist only for the 0th order (when $n = n' = 0$), as otherwise several combinations of coefficients may be solution to the boundary problem. In particular, the integration of first degree polynomials on a surface can lead to null columns in the matrix. Therefore, for the boundary only, only the 0th order terms are computed while the other components are set to 0.

The momentum corresponding condition is derived using Eq. 6}:

$$ p^{\alpha n} = \rho \sum_{n'} I^{\alpha n n'} \sum_{n"} W_S^{\alpha n n"} \int_{\Gamma_D} \dot{u_D} p^{\alpha n"} \, ds $$

Neumann BC

We consider a Lagrangian (with *u* as an additional variable for the strain-based formulation, not necessary for the displacement-based one):

$$ L(\boldsymbol{v}, \boldsymbol{\epsilon}, \boldsymbol{u}) = \int_V \frac{1}{2} \rho \boldsymbol{v}^2 dV - \frac{1}{2} \boldsymbol{\epsilon} : \boldsymbol{C} : \boldsymbol{\epsilon} \, dV + \int_{\Gamma_N} T_N . u \, ds $$

In PDS-FEM formalism, applying the Hamilton's principle leads to the updated Euler-Lagrange equation:

$$ \frac{d}{dt} \frac{\partial L}{\partial v^{\alpha n}} - \sum_{\beta, m} {}^{t}\tilde{B}^{\beta\alpha m n} . \frac{\partial L}{\partial \epsilon^{\beta m}} - \int_{\Gamma_N} T_N . P^{\alpha n} \, ds = 0 $$

adding the term $\int_{\Gamma_N \cap \Phi^{\alpha}} T_N . P^{\alpha n} \, ds$ to the calculation of $\dot{p}^{\alpha n}$ in the Hamiltonian systems.

References

[1]Ferté, G., Massin, P., & Moes, N. (2016). 3D crack propagation with cohesive elements in the extended finite element method. *Computer Methods in Applied Mechanics and Engineering*, *300*, 347-374.

[2]Chen, L., Rabczuk, T., Bordas, S. P. A., Liu, G. R., Zeng, K. Y., & Kerfriden, P. (2012). Extended finite element method with edge-based strain smoothing (ESm-XFEM) for linear elastic crack growth. *Computer Methods in Applied Mechanics and Engineering*, *209*, 250-265.

[3] Moës, N., Gravouil, A., & Belytschko, T. (2002). Non-planar 3D crack growth by the extended finite element and level sets—Part I: Mechanical model. *International journal for numerical methods in engineering*, *53*(11), 2549-2568.

[4] Cockburn, B. (2003). Discontinuous galerkin methods. *ZAMM-Journal of Applied Mathematics and Mechanics/Zeitschrift für Angewandte Mathematik und Mechanik: Applied Mathematics and Mechanics*, *83*(11), 731-754.

[5] Seagraves, A., & Radovitzky, R. (2015). Large-scale 3D modeling of projectile impact damage in brittle plates. *Journal of the Mechanics and Physics of Solids*, *83*, 48-71.

[6] Bede, N., Ožbolt, J., Sharma, A., & İrhan, B. (2015). Dynamic fracture of notched plain concrete beams: 3D finite element study. *International Journal of Impact Engineering*, *77*, 176-188.

[7] Hori, M., Oguni, K., & Sakaguchi, H. (2005). Proposal of FEM implemented with particle discretization for analysis of failure phenomena. *Journal of the Mechanics and Physics of Solids*, *53*(3), 681-703.

[8] Pal, M. K., Wijerathne, L., Hori, M., & Ichimura, T. (2015). Simulation of cracks in linear elastic solids using higher order Particle Discretization Scheme-FEM. *Journal of Japan Society of Civil Engineers A2 (Applied Mechanics) 71*(2), I_327-I_337.

[9] Pal, M. K., Wijerathne, L., Hori, M., Ichimura, T., & Tanaka, S. (2014). Implementation of finite element method with higher order particle discretization scheme. *Journal of Japan Society of Civil Engineers A2 (Applied Mechanic)*, *70*(2), I_297-I_305.

[10]Wijerathne, M. L. L., Oguni, K., & Hori, M. (2009). Numerical analysis of growing crack problems using particle discretization scheme. *International journal for numerical methods in engineering*, *80*(1), 46-73.

[11] Hori, M., Wijerathne, M. L. L., Riaz, M., & Ichimura, T. (2018). Rigorous derivation of hamiltonian from lagrangian for solid continuum. *Journal of Japan Society of Civil Engineers A2 (Applied Mechanics) 6*(1), 1-11.

[12] Burridge, R. (1973). Admissible speeds for plane-strain self-similar shear cracks with friction but lacking cohesion. *Geophysical Journal International*, *35*(4), 439-455.

[13] Andrews, D. J. (1976). Rupture velocity of plane strain shear cracks. *Journal of Geophysical Research*, *81*(32), 5679-5687.

[14] Das, S., & Aki, K. (1977). A numerical study of two-dimensional spontaneous rupture propagation. *Geophysical journal international*, *50*(3), 643-668.

[15] Rosakis, A. J., Samudrala, O., & Coker, D. (1999). Cracks faster than the shear wave speed. *Science*, *284*(5418), 1337-1340.

[16] Xia, K., Rosakis, A. J., & Kanamori, H. (2004). Laboratory earthquakes: The sub-Rayleigh-to-supershear rupture transition. *Science*, *303*(5665), 1859-1861.

[17] Archuleta, R. J. (1984). A faulting model for the 1979 Imperial Valley earthquake. *Journal of Geophysical Research: Solid Earth*, *89*(B6), 4559-4585.

[18] Bouchon, M., Bouin, M. P., Karabulut, H., Toksöz, M. N., Dietrich, M., & Rosakis, A. J. (2001). How fast is rupture during an earthquake? New insights from the 1999 Turkey earthquakes. *Geophysical Research Letters*, *28*(14), 2723-2726.

[19] Bouchon, M., & Vallée, M. (2003). Observation of long supershear rupture during the magnitude 8.1 Kunlunshan earthquake. *Science*, *301*(5634), 824-826.

[20] Ellsworth, W. L., Celebi, M., Evans, J. R., Jensen, E. G., Kayen, R., Metz, M. C., ... & Stephens, C. D. (2004). Near-field ground motion of the 2002 Denali Fault, Alaska, earthquake recorded at Pump Station 10. *Earthquake spectra*, *20*(3), 597-615.

[21] Socquet, A., Hollingsworth, J., Pathier, E., & Bouchon, M. (2019). Evidence of supershear during the 2018 magnitude 7.5 Palu earthquake from space geodesy. *Nature Geoscience*, *12*(3), 192.

[22] Hairer, E., Lubich, C., & Wanner, G. (2006). *Geometric numerical integration: structure-preserving algorithms for ordinary differential equations* (Vol. 31). Springer Science & Business Media.